The FEBS Journal

FEBS PRESS science publishing by scientists

Characterization of a glycoside hydrolase endolysin from *Acinetobacter baumannii* phage *Ab*TZA1 with high antibacterial potency and novel structural features

Georgios E. Premetis[1], Angeliki Stathi[2], Anastassios C. Papageorgiou[3] and Nikolaos E. Labrou[1]

1 Laboratory of Enzyme Technology, Department of Biotechnology, School of Applied Biology and Biotechnology, Agricultural University of Athens, Greece
2 Department of Microbiology, 'Aghia Sophia' Children's Hospital, Athens, Greece
3 Turku Bioscience Centre, University of Turku and Åbo Akademi University, Finland

Keywords
Acinetobacter baumannii; antibacterial; endolysin; enzybiotics; enzyme engineering

Correspondence
N. E. Labrou, Laboratory of Enzyme Technology, Department of Biotechnology, School of Applied Biology and Biotechnology, Agricultural University of Athens, 75 Iera Odos Street, GR-11855-Athens, Greece
Tel: +302105294308
E-mail: lambrou@aua.grand
A. C. Papageorgiou, Turku Bioscience Centre, University of Turku and Åbo Akademi University, Turku 20521, Finland
Tel: +358294503752
E-mail: anapap@utu.fi

(Received 19 September 2022, revised 11 November 2022, accepted 18 November 2022)

doi:10.1111/febs.16686

The classification of *Acinetobacter baumannii* by WHO as 'priority 1' antibiotic-resistant pathogen underlines the urgent need for novel antimicrobial agents towards this pathogen. In this work, screening of the *A. baumannii* phage *Ab*TZA1 genome allowed the identification of a putative endolysin (*Ab*Lys1, EC3.2.1.17) that belongs to the glycoside hydrolase family 24 (GH24). The sequence of *Ab*Lys1 was cloned, expressed in *E. coli* and purified. The lytic activity and specificity of *Ab*Lys1 were evaluated against a range of Gram-positive and Gram-negative human pathogens. *Ab*Lys1 was found to display a high selectivity towards *A. baumannii*. Kinetic analysis was carried out to characterize the dependence of its lytic activity on pH. The enzyme shows its maximal activity at pH values 7–8. The structure of *Ab*Lys1 was determined by X-ray crystallography to 1.82 Å resolution. The overall structure revealed two helical domains: a small, antenna-like, N-terminal domain and a larger C-terminal domain with six α-helices and a β-hairpin. Both the antenna-like and β-hairpin regions contain short sequences (AMseq1 and AMseq2) with predicted antimicrobial activity. Engineering studies revealed a key role of AMseq1 and AMseq2 on the enzyme's lytic activity towards *A. baumannii* cells but not towards purified peptidoglycan. This suggests that both sequences affect the destabilization of the outer membrane, thus providing access of the catalytic domain to the peptidoglycan. In addition, the deletion of AMseq1 enhanced the enzyme stability, whereas the deletion of AMseq2 diminished it. The results suggest that *Ab*Lys1 is a promising new enzybiotic with efficient lytic and antimicrobial activity.

Introduction

The World Health Organization (WHO) has raised many concerns about the emergence and spread of antibiotic-resistant pathogens that have acquired new resistance mechanisms (https://www.who.int/health-topics/antimicrobial-resistance). Based on estimates from 204 countries and territories, 1.27 million deaths

Abbreviations
AM, antimicrobial peptide; CAZy, Carbohydrate Active Enzymes Database; CDD, Conserved Domains Database; DAPI, 4′,6-diamidino-2-phenylindole; DSF, differential scanning fluorimetry; EthD-III, Ethidium Homodimer III; GEWL, goose egg-white lysozymes; HEWL, hen egg-white lysozymes; MBC, minimal inhibition concentration (MIC) bactericidal concentration; MH, Mueller–Hinton; MIC, minimum bactericidal concentration; MurNAc, *N*-acetylmuramic acid; PNG, peptidoglycan; RBBR, Remazol Brilliant Blue-R; RBBR-PNG, RBBR-labelled Peptidoglycan; SLT, soluble lytic transglycosylases; WGA, wheat germ agglutinin; WHO, World Health Organisation.

in 2019 have been attributed directly to antibiotic-resistant bacteria [1] and predictions about the future are ominous as 10 million deaths per year could result from resistant pathogens by 2050 [2].

Acinetobacter baumannii is a Gram-negative bacterium that has been classified by WHO as 'priority 1' antibiotic-resistant pathogen alongside *Pseudomonas aeruginosa* and *Enterobacteriaceae* [3]. *A. baumannii* is considered the most infectious and dangerous pathogen inside hospital environments worldwide [4–6]. This opportunistic pathogen causes community and nosocomial infections, predominantly ventilator-associated pneumonia, bloodstream, urinary tract and skin and soft tissue infections, especially among critically ill patients in intensive care units [7,8]. The mechanisms involved in the establishment and progression of *A. baumannii* infections are still unclear. However, some strains possess genes coding for pilus biogenesis, iron uptake and metabolism, quorum sensing [9] or the production of lipid A, a lipid component of an endotoxin responsible for the toxicity of Gram-negative bacteria by inducing a pro-inflammatory cytokine expression in human monocytes mediated by the CD14 receptor [10–12]. During the COVID-19 pandemic, coinfections with *A. baumannii* strains secondary to SARSCoV-2 infections were reported multiple times in the literature. Incidences of secondary infections (mainly lower respiratory tract infections) attributed to *A. baumannii* were reported to be approximately 1% of hospitalized COVID-19 patients in hospitals worldwide [13–15].

Antibiotic resistance is a complex problem that requires novel approaches in confronting multidrug pathogens. Although the field of phage therapy, which exploits bacteriophages for the treatment of bacterial infections, has been thoroughly investigated for almost a century [16], the antibacterial potential of phage-encoded endolysins has gained increasing interest only during the last two decades [17]. Endolysins (enzybiotics), therefore, represent an interesting new-yet-old weapon in the fight against resistant bacteria [18,19]. Their primary function is to hydrolyse the peptidoglycan cell wall of bacteria during the lytic cycle of bacteriophages [20]. Degradation of the cell wall leads to osmotic shock, disruption and usually to bacterial death [21]. Based on their catalytic mechanisms, peptidoglycan hydrolases are classified into amidases, peptidases and glycosidases [22,23]. Glycosidases or glycoside hydrolases hydrolyse the 1,4-beta linkages between *N*-acetyl-D-glucosamine and *N*-acetylmuramic acid in peptidoglycan heteropolymers of peptidoglycan. These enzymes have significant structural differences but are classified into two large categories: *N*-acetylglucosaminidases and lysozymes [24]. LysAB54 [25], LysMK34 [26] and Abp013 [27] are examples of bacteriophage endolysins with high antibacterial activity against a wide range of *A. baumannii* strains.

In the present work, a putative endolysin (*Ab*Lys1) was identified and characterized. *Ab*Lys1 was evaluated for its antimicrobial activity against a clinically isolated *A. baumannii* strain. The work aimed at the discovery of new antimicrobial agents towards *A. baumannii* cells as an alternative non-antibiotic strategy to combat this antibiotic-resistant pathogen.

Results and Discussion

Identification and *in silico* characterization of *Ab*Lys1

The Acinetobacter phage AbTZA1 (MK278860) with high lytic activity towards *A. baumannii* strains has been previously isolated from sewage and found to belong to the Myoviridae family [28]. Its available genome was searched for endolysin-like open reading frames (ORF) encoding for a hypothetical glycoside hydrolase-like protein using as a query the sequence of bacteriophage T4 type endolysin. A putative gene (accession no: AZU98615.1) (*Ab*Lys1) was selected for further study. The *Ab*Lys1 gene consists of 582 bp that encodes for a protein of 193 amino acids with predicted molecular mass and isoelectric point of 21.61 kDa and 8.32, respectively.

The sequence of *Ab*Lys1 belongs to the cd00737 (endolysin and autolysin) family in the Conserved Domains Database (CDD, https://www.ncbi.nlm.nih.gov/cdd/). This family is a member of the heterogenous Lyz-like cl00222 superfamily that contains several members, including soluble lytic transglycosylases (SLT), goose egg-white lysozymes (GEWL), hen egg-white lysozymes (HEWL), chitinases, bacteriophage lambda lysozymes, endolysins, autolysins, chitosanases and pesticin. Endolysins with the endolysin/autolysin domain (CDD id cd00737) are mainly originated from phages and prophages integrated into Gram-negative bacterial genomes.

Phage endolysins that infect Gram-negative bacteria show a more globular architecture composed of a single catalytic domain [29]. In particular, domains that belong to the lysozyme-like family (cl00222, cd00442), bacteriophage lambda lysozyme domain family (cd00736) and endolysin/autolysin domain family (cd00737) represent typical domains for Gram-negative bacteria. On the other hand, domains that belong to the GH25 muramidase 1 (cd06413) family and alanine amidases of the MurNAc-LAA (cl02713) superfamily are specific for Gram-positive bacteria [24,30,31].

BLASTp search of the NCBI protein sequence database using as a query the *Ab*Lys1 protein allowed the construction of a phylogenetic tree (Fig. 1A) using the resulting hits. The sequences were clustered into two separate clades. The first clade contains endolysins originated from phages and the second large clade includes all other autolysins from phages and prophages integrated into the genomes of Gram-negative bacteria.

Analysis of the *Ab*Lys1 sequence using the Carbohydrate Active Enzymes Database (CAZy; http://www.cazy.org/) showed that *Ab*Lys1 displays high homology with enzymes classified into the glycoside hydrolase family 24 (GH24). According to the classification, the predicted function of *Ab*Lys1 is the hydrolysis of the 1,4-beta linkages between *N*-acetyl-D-glucosamine (NAG) and *N*-acetylmuramic acid (NAM) in peptidoglycan heteropolymers in *Acinetobacter* cells.

Amino acid sequence alignment of close homologue endolysin and autolysin sequences (> 67% homology) with two endolysins that belong to the T4 lysozyme-like family of proteins with confirmed lysozyme activity is depicted in Fig. 1B. The alignment allowed the identification of the conserved catalytic triad (Glu52, Asp61 and Thr67) based on the sequence identity with the bacteriophage T4 lysozyme (PDB id 2lzm) and muramidase from *A. baumannii* AB 5075UW prophage (PDB id 6et6) [32] (Fig. 1B). The catalytic triad in *Ab*Lys1 is conserved, suggesting that the catalytic mechanism of peptidoglycan degradation is the same as that of the T4 lysozyme, the archetype of the GH24 family.

Cloning, expression and purification of recombinant *Ab*Lys1

The gene of the *Ab*Lys1 was codon optimized, synthesized and subcloned into the T7 expression plasmid pETite fused with a 6xHis tag at its C terminus. The plasmid was used to transform the expression of host *E. coli* BL21 (DE3). The 6xHis tag enabled *Ab*Lys1 to be effectively purified by immobilized metal ion affinity chromatography on Ni^{+2}-IDA-Sepharose affinity column (Fig. 2). The fractions with the highest purity (elution fractions with 0.15–0.35 M imidazole) were mixed and stored at 4 °C for further study.

Biochemical properties and lytic activity of the purified *Ab*Lys1

Lytic activity of the purified AbLys1

To demonstrate that *Ab*Lys1 is an active endolysin, the lytic activity of the recombinant protein was evaluated using turbidity assays. The most common assay for determining the endolysin's activity is based on the drop in optical density of the substrate after the addition of the enzyme [29,33]. Thus, the activity of *Ab*Lys1 was determined using a turbidity assay from time-dependent turbidity changes in a suspension of Remazol Brilliant Blue-R-labelled peptidoglycan (RBBR-PNG) (Fig. 2B,C) or *A. baumannii* cells suspensions (Fig. 2D,E). The results showed that *Ab*Lys1 can increase the turbidity of RBBR-PNG, suggesting an active peptidoglycan lytic enzyme. The specificity of *Ab*Lys1 was further assessed by employing a range of different bacterial strains (*E. faecium*, *S. aureus*, *S. pyogenes*, *B. cereus* and *C. difficile*) using the cell suspension turbidity reduction assay. The results (Fig. 3) showed that the enzyme exhibits significantly higher lytic activity against the clinical strain *A. baumannii*, compared to other species, suggesting a higher preference and presumably enhanced specificity for *A. baumannii*, the native host of the bacteriophage *Ab*TZA1 [34–36].

Measurement of glycosidase activity of AbLys1

As already mentioned, the enzyme belongs to the GH24 family. The enzyme was therefore tested *in vitro* for glycosidase activity using the Park & Johnson method [37]. Thus, *A. baumannii* cell walls were treated with *Ab*Lys1 for 2 h at 25 °C in HEPES buffer 0.05 M, pH 7.5. The results, listed in Table 2, demonstrated that digestion was clearly accompanied by an increase in reducing groups compared to the control incubation in the absence of *Ab*Lys1.

Effect of pH on the enzyme activity

The effect of pH on the activity of *Ab*Lys1 was studied using the RBBR-PNG assay and different buffers, covering the pH range of 4–10. As shown in Fig. 4A, the curve of the enzyme activity versus pH displays a bell-shaped dependence. The highest enzyme activity was observed between pH values 7–8. The activity was significantly decreased below pH 6.0 and above pH 8.0. The bell-shaped dependence of activity data on pH allowed the prediction of the pK_a of the ionizable enzyme's groups that are involved in catalysis. The pH dependence shown in Fig. 4A suggests that an acidic and basic group with approximately pK_a 5.9 and 8.9 are involved in catalysis. Although the assignment of these pK_as to specific amino acid residues is difficult, we can nevertheless speculate that the pK_a 5.9 probably corresponds to one of the active site residues, either Glu52 or Asp61. Previously published

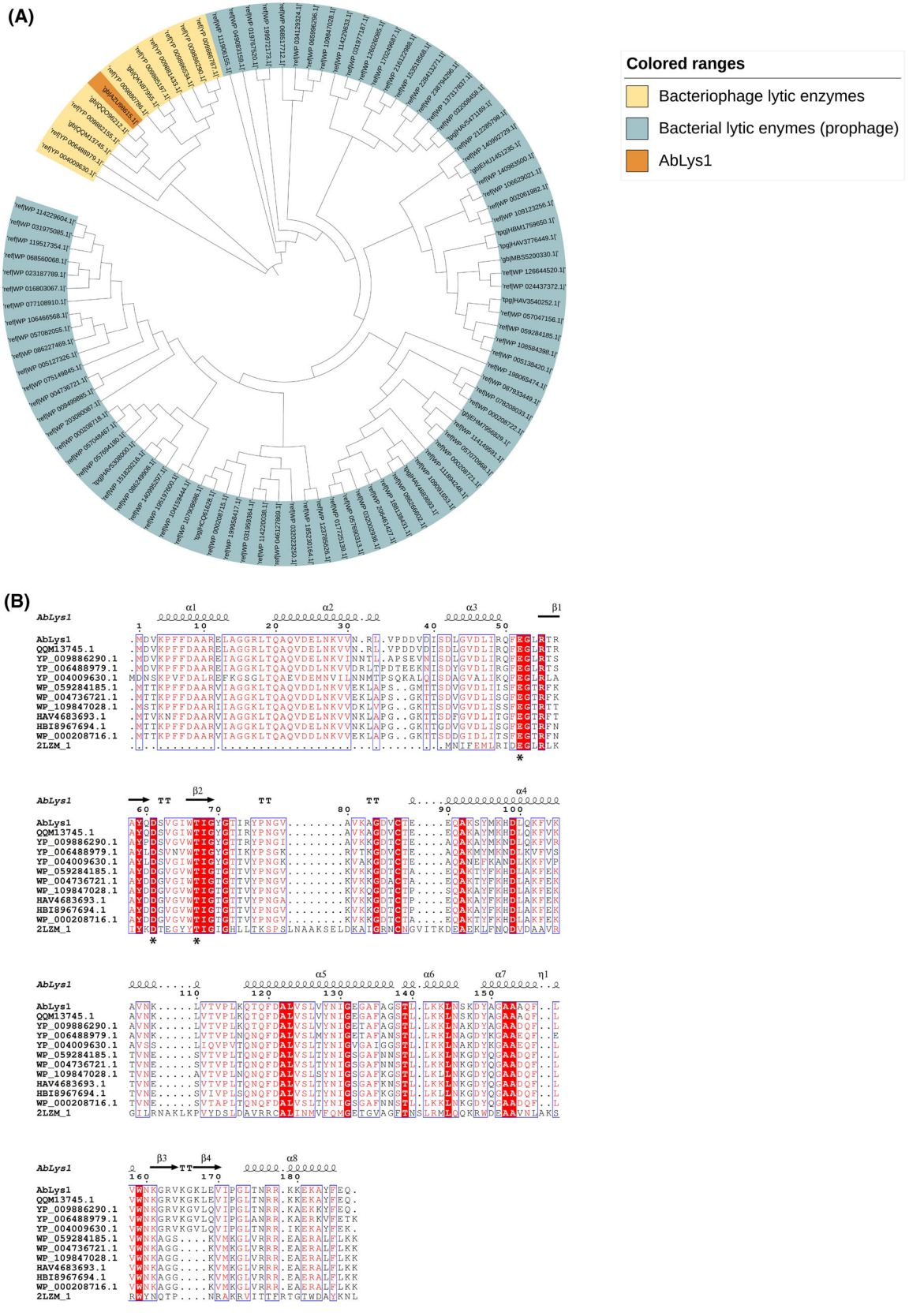

Fig. 1. (A) Phylogenetic analysis of *Ab*Lys1. (B) Multiple sequence alignment of homologous sequences with *Ab*Lys1. Alignment was performed using CLUSTALO and displayed using ESPRIPT 3.0 [74]. The sequences used were the following: NCBI accession number: YP_006488979.1 (putative lysozyme from Acinetobacter phage ZZ1), WP_109847028.1 (lysozyme from *A. baumannii*), WP_059284185.1 (lysozyme from *A. baumannii*), WP_004736721.1 (lysozyme from *A. baumannii*), HAV4683693.1 (glycoside hydrolase family protein from *A. baumannii*), HBI8967694.1 (lysozyme from *A. baumannii*), YP_004009630.1 (putative lysozyme from Acinetobacter phage Acj61), QQM13745.1 (endolysin–lysozyme murein hydrolase from Acinetobacter phage Maestro), YP_009886290.1 (lysozyme from Acinetobacter phage vB_AbaM_Apostate), *Acinetobacter baumannii* muramidase (WP_000208716), bacteriophage T4 lysozyme (PDB: 2LZM_1) and *Ab*Lys1 (Acinetobacter phage TZA1, accession code: AZU98615.1). Conserved residues that form the putative catalytic site are shown as stars.

investigations have shown that in the case of lysozyme, its acidic catalytic residues, Asp 52 and Glu35, display discrete ionizable properties. pH studies in lysozyme showed that their side chains display pK_as of 3.5 and 6.3, respectively. Asp52 is surrounded by polar groups in contrast to Glu35 which is located in a more hydrophobic environment. Consequently, the pK_a of Glu35 is elevated [38,39]. The sharp transition observed in the alkaline pH range (Fig. 4A) suggests that a basic group (e.g. $-NH_2$ group) presumably needs to be protonated (positively charged) for efficient catalysis. Its ionization dramatically affects catalysis, leading to an inactive enzyme. The pK_a 8.9 is close to that expected by an ε-amino group of a Lys residue.

Structural stability of AbLys1

The structural stability of *Ab*Lys1 was investigated using two complementary approaches, namely differential scanning fluorimetry (DSF) and thermal

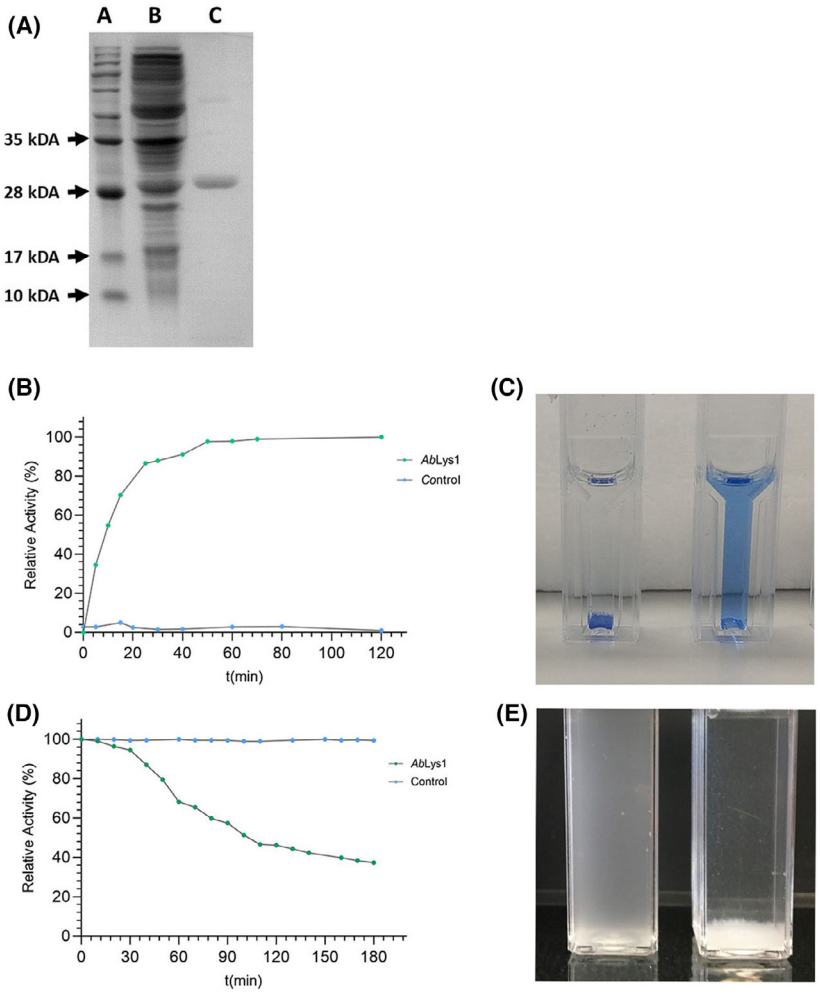

Fig. 2. (A) SDS/PAGE analysis of *Ab*Lys1 purification. Protein bands were stained with Coomassie Brilliant Blue R-250. Lane A, Protein Ladder. Lane B, *E. coli* BL21 (DE3) crude extract after induction with IPTG (1 mM); Lane C, *Ab*Lys1 purified by affinity chromatography on Ni^{+2}-IDA-Sepharose. (B) Enzyme activity of the recombinant *Ab*Lys1. Enzyme activity was demonstrated by measuring the time-dependent increase in absorbance using RBBR-PNG as substrate. Changes in absorbance were measured at 595 nm at regular time intervals and a fixed temperature (25 °C), using purified *Ab*Lys1 ●, or in the absence of the enzyme ○. (C) Visual inspection of the released dye from the RBBR-PNG complex after the end of the enzyme reaction. (D) Enzyme activity was demonstrated by measuring the time-dependent turbidity changes in a suspension of *A. baumannii* cells. Changes in turbidity were measured spectrophotometrically at 600 nm at regular time intervals and a fixed temperature (25 °C), using purified *Ab*Lys1 ●, or in the absence of the enzyme ○. (E) Visual inspection of the reduction in the turbidity of the *A. baumannii* cells after the end of the enzymatic reaction.

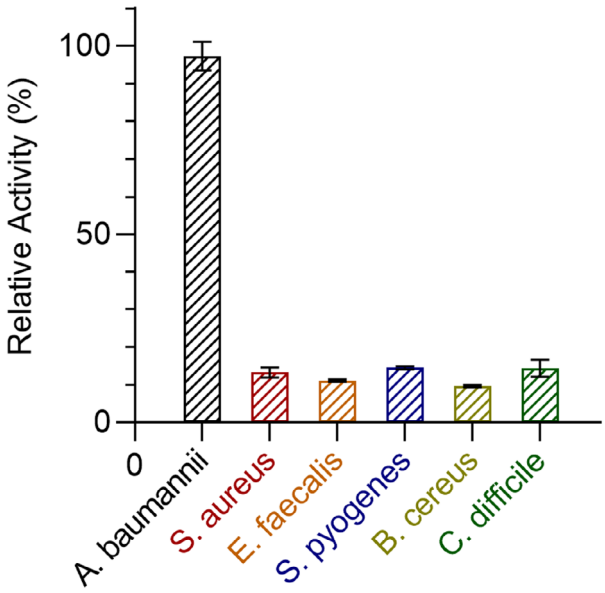

Fig. 3. Activity of *Ab*Lys1 against representative bacterial strains. Enzyme activity was demonstrated by measuring the time-dependent turbidity changes in a suspension of the bacterial cells. Changes in turbidity were measured at 600 nm at a fixed temperature (25 °C) using purified *Ab*Lys1, and were compared to a negative control in the absence of the enzyme. The relative enzyme activity was calculated by setting the activity of *Ab*Lys1 as 100%. Error bars represent the estimated standard deviation.

Table 1. X-ray data processing and refinement statistics.

	*Ab*Lys1
Data processing	
Beamline	P13 (EMBL, Hamburg)
Wavelength (Å)	0.8266
Resolution (Å)	46.73–1.82 (1.88–1.82)
Space group	$P2_1$
Unit cell	
a, *b*, *c* (Å)	41.6, 184.8, 57.9
β (°)	110.7
No. molecules/asymmetric unit	4
Observations	459 501 (14 225)
No. of unique reflections	70 067 (4406)
Completeness (%)	96.2 (61.6)
Multiplicity	6.6 (3.2)
Mosaicity (°)	0.15
R_{meas}	0.078 (1.276)
$CC_{1/2}$	0.999 (0.424)
Mean [$I/\sigma(I)$]	12.5 (0.8)
Wilson B factor (Å^2)	34.5
Refinement	
No. of reflections used	69 947
R_{cryst}/R_{free}	0.221/0.256
RMSD in bonds (Å)	0.008
RMSD in angles (°)	0.952
No. of water molecules	548
Average B-factor (Å^2)	29.9
Ramachandran favoured/outliers (%)	97.0/0.3
Clashscore	6.2
PDB id	8app

Table 2. Glycosidase activity of *A. baumannii* phage *Ab*Lys1.

Incubation mixture	Reducing activity (μg glucose; mean ± SD)
A. baumannii cell walls with *Ab*Lys1	3.49 ± 0.21
A. baumannii cell walls without *Ab*Lys1	0.08 ± 0.002

inactivation. DSF explores the change in the fluorescence of SYPRO orange when it binds to the denatured enzyme during heat treatment (25–95 °C) at optimum activity conditions (HEPES, 0.05 M, pH 7.5). Fig. 5A shows the denaturation curve of *Ab*Lys1. The melting temperature was 45.81 ± 0.03 °C, suggesting a good thermal stability for *Ab*Lys1 comparable to that observed for other bacteriophage endolysins [40,41].

The thermal inactivation of *Ab*Lys1 was also investigated by measuring the residual enzyme activity after incubation of the enzyme at different temperatures (4–60 °C) for 10 min. The results (Fig. 5B) showed that the activity of *Ab*Lys1 remained unaffected below 20 °C. However, its activity rapidly declined at higher temperatures with a sharp transition between 40 and 50 °C.

Evaluation of inhibitory and bactericidal activity of AbLys1 against live cultures of *A. baumannii* cells

The effect of purified *Ab*Lys1 on live cultures of *A. baumannii* cells was evaluated by fluorescence microscopy. The bacterial viability, following *Ab*Lys1 treatment, was assessed using a Gram Stain Kit that provides a reliable assay for distinguishing live (blue) versus dead (red) *A. baumannii* cells. As shown in Fig. 6, incubation of live cultures of *A. baumannii* cells with 150 μg *Ab*Lys1 for 5 h at 25 °C caused the appearance of red dyed cells suggesting a significant antibacterial activity of *Ab*Lys1 on live *A. baumannii* cells.

For further evaluation of the bactericidal activity of *Ab*Lys1, the disk diffusion method against the *A. baumannii* clinical strain was used (Fig. 7A). The results showed that inhibition of *A. baumannii* growth occurs between 10 and 60 μg of *Ab*Lys1. However, significant inhibition was observed at 40 and 60 μg of *Ab*Lys1, where the diameter of the inhibition zone was 19.7 and 23.3 mm, respectively. The broth dilution method was

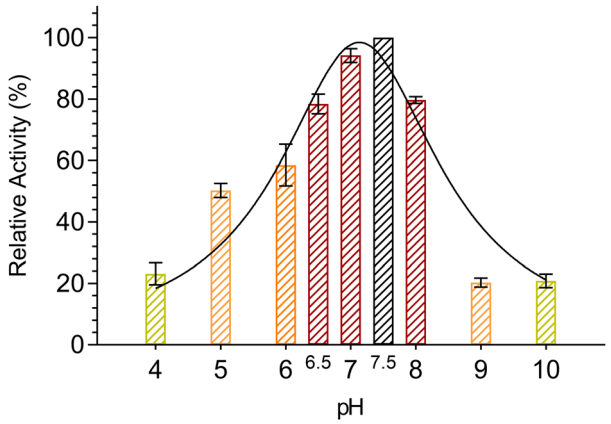

Fig. 4. Effect of pH on the activity of *Ab*Lys1. Bar charts show the enzyme's relative lytic activity against the RBBR-labelled peptidoglycan of *A. baumannii*. Experiments were performed at 25 °C for 120 min using 150 μg of protein. Error bars represent the estimated standard deviation.

also used, and the results are shown in Fig. 7B. A dose–response effect of enzyme concentration on the number of colonies formation was observed. In particular, < 50 μg of *Ab*Lys1 appears to be effective for lowering > 50% the number of *A. baumannii* colonies, suggesting an efficient bactericidal activity. The use of higher amount of enzyme (500 μg) results in zero colony formation.

Crystal structure analysis of *Ab*Lys1

*Ab*Lys1 was crystallized with four molecules in the asymmetric unit (Fig. 8A). All molecules have the same overall fold and only subtle differences. The structure of *Ab*Lys1 revealed two helical domains: a small, antenna-like, N-terminal domain with two α-helices (α1 and α2) and a larger C-terminal domain with six α-helices and two short β-strands that form a β-hairpin. The two domains are connected via a 5-residue linker that shows an extended conformation. The overall α-helical pattern of the C-terminal domain is typical of the glycoside hydrolase family GH24 with lysozyme activity [32]. The putative active site is formed by the three conserved catalytic amino acids (Glu52, Asp61 and Thr67) identified through the bioinformatics analysis (Fig. 1B). These residues are clearly seen in the active site (Fig. 8B). Inspection of the active site shows that Asp61 and Thr67 are located in a loop (Fig. 8B) characterized by length variability among other enzymes of the GH24 family, such as the P1 phage endolysin Lyz (PDB id 1xjt; corresponding residues Asp58 and Thr67) [42] and *Acinetobacter baumannii* muramidase (PDB id 6et6; Asp73 and Thr79) [32]. It can therefore be suggested that conformational changes would be required to bring the catalytic triad to the right position for catalysis [43]. The catalytic mechanism of *Ab*Lys1 is presumably similar to that of GH24 peptidoglycan hydrolases that target the β-1,4 glycosidic bond between NAM and NAG. The hydrolytic mechanism (based on that of T4 lysozyme) can be summarized as follows: Glu52 is suggested to protonate the glycosidic oxygen while the deprotonated carboxylate of Asp61 performs a nucleophilic attack on the carbon of the C1-O4 bond in the NAM-NAG connection and Thr67 through resonance stabilizes the carbon of the C1-O4 bond [44,45]. pH studies (Fig. 4A) showed that two transitions with pK_as of 5.9 and 8.9 are involved in catalysis. Asp61 is exposed to the solvent and surrounded by polar groups; however, Glu52 is located in a more hydrophobic environment.

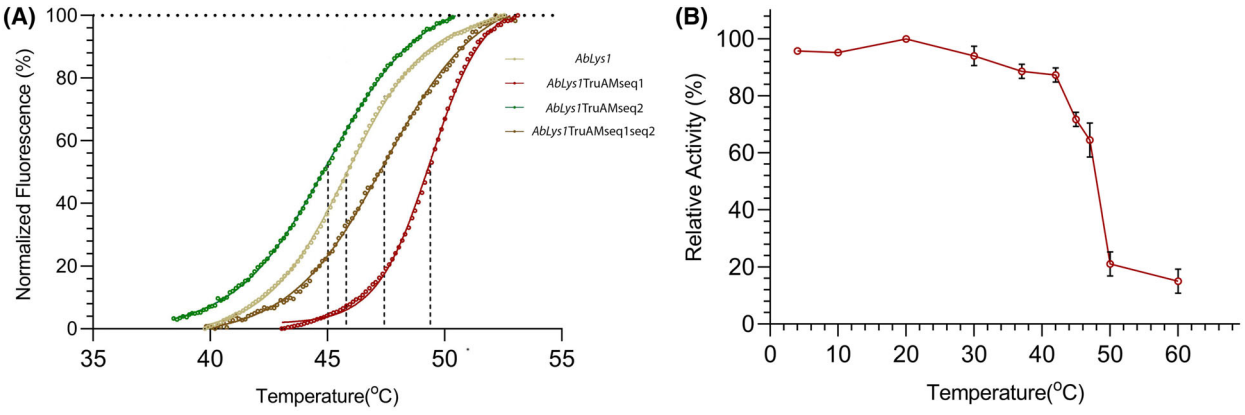

Fig. 5. Thermal stability of *Ab*Lys1. (A) DSF curve of *Ab*Lys1 and the truncated engineered variants for the determination of melting temperatures (T_m). (B) Thermal inactivation of *Ab*Lys1. The enzyme was incubated at different temperatures for 10 min and its residual activity was evaluated. Error bars represent the estimated standard deviation.

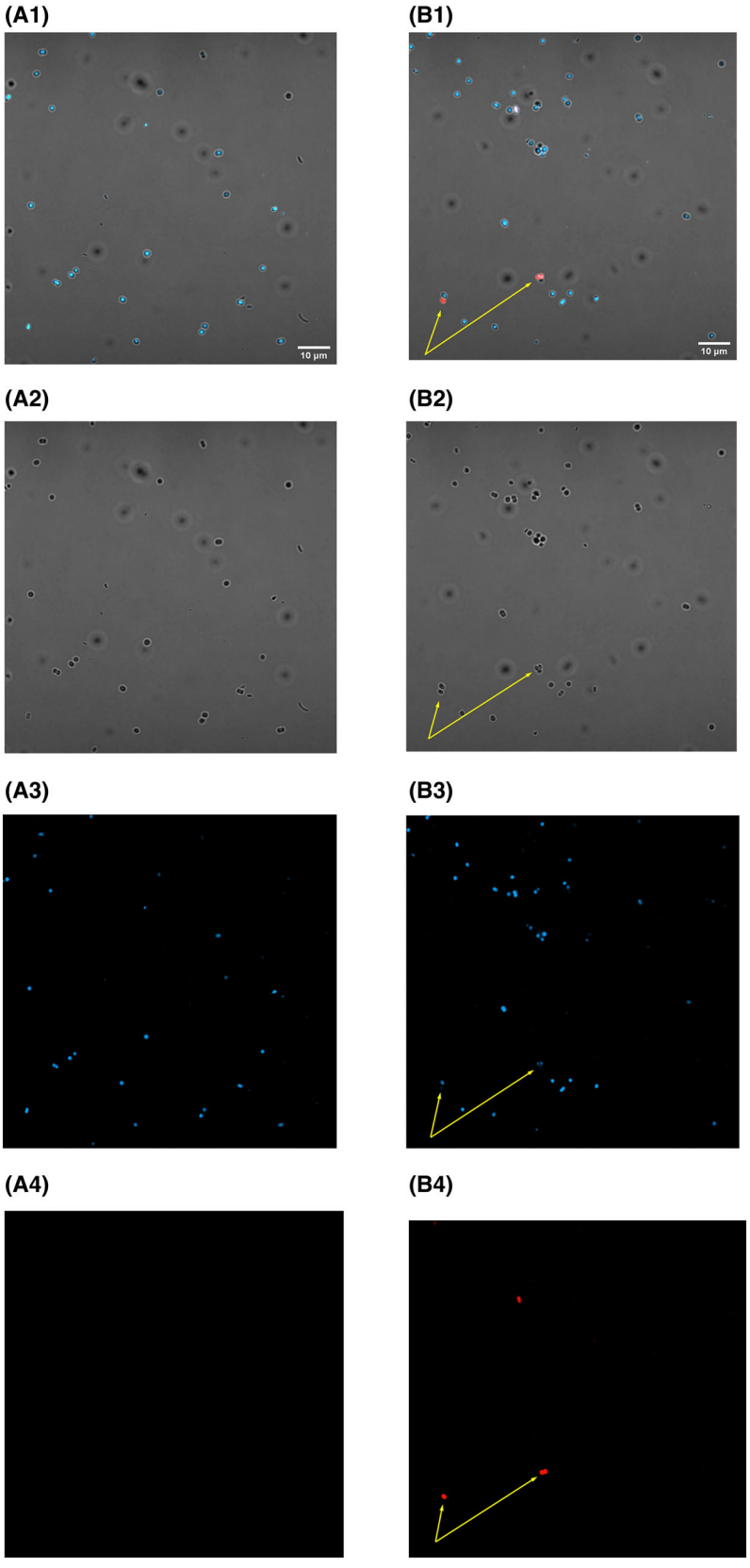

Fig. 6. Assessment of the morphology of *A. baumannii* using fluorescent microscopy. (A1–4) are images of *A. baumannii* (control) without treatment with *Ab*Lys1. (B1-4) are images of *A. baumannii* (test) treated with *Ab*Lys1. A1: superimposed image of A2, A3, A4. B1: superimposed image of B2, B3, B4. A2 and B2 represent transmitted light images of *A. baumannii*. A3, B3 represent images of *A. baumannii* stained with DAPI dye. A4, B4 represent images of *A. baumannii* treated with EthD-III dye. Treated and untreated cells were stained with DAPI (blue). Only the *Ab*Lys1 treated *A. baumannii* were stained with EthD-III (red) as a results of membrane compromisation. Yellow arrows indicate dead cells. The scale bar indicates the length of 10 μm.

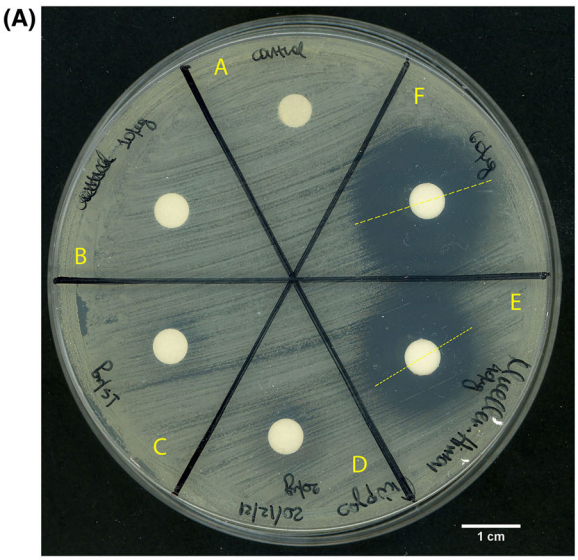

Fig. 7. (A) Disk diffusion method using different amounts (μg) of *Ab*Lys1. (A) 0 μg (control), (B) 10 μg, (C) 15 μg, (D) 20 μg, (E) 40 μg and (F) 60 μg. A clear zone of growth inhibition is observed around the discs with 40 and 60 μg of *Ab*Lys1. The scale bar indicates the length of 1 cm. (B) Broth dilution method using different amounts (μg) of AbLys1. (A) 0 μg (control), (B) 50 μg, (C) 100 μg, (D) 150 μg, (E) 250 μg and (F) 500 μg of *Ab*Lys1, respectively.

Consequently, the pK_a of Glu52 is possibly elevated, making it a better general acid at higher pH values and less likely to donate a proton and acquire a negative charge at low pH values. Similar observations have also been reported in the case of chicken lysozyme, where a pK_a of 6.3 has been determined for Glu35 [38,39].

It has been proposed that the distance between the catalytic Glu and Asp is a distinguishing feature of the catalytic mechanism of bacteriophage endolysins and characterizes whether the anomeric centre of the cleaved peptidoglycan glycoside is retained or inverted [46]. An average distance of 4.3–5.9 Å is observed in enzymes that retain the anomeric centre and 7.2–9.5 Å is typically observed when the anomeric centre is inverted. The catalytic residues Glu and Asp of *Ab*Lys1 are positioned 10.9 Å apart, consistent with a peptidoglycan hydrolase that inverts the anomeric centre of the peptidoglycan glycoside during catalysis, similar to that of T4 lysozyme [47]. The active site of *Ab*Lys1 contains also Tyr128 and Asn129 that are structurally equivalent to Phe104 and Gln105 which have been implicated in NAG-NAM binding in T4 lysozyme [32], thus further supporting the predicted specificity for *Ab*Lys1.

Structure comparison using PDBePISA showed similarities with the muramidase domain of *Asticcacaulis excentricus* Spmx (PDB id 6h9d) [48] with an RMSD of 1.34 Å for 133 aligned pairs (40% sequence identity) (Fig. 8C). The loop structure appears to control the width of the catalytic cavity. The N-terminal helical domain is absent in the deposited structures and its role needs to be investigated. Full-length endolysin R21 from phage 21 (PDB id 3hde) and *E. coli* DLP12 endolysin (4zpu) have an extra N-terminal helix, which is close to the first helix of the muramidase domain (corresponds to α3 in *Ab*Lys1) and both helices form a special signal-arrest-release (SAR) domain [49] that helps to anchor endolysin P21 to cell membranes. The N-terminal helical domain may therefore undergo a conformation change that could bring it close to the C-terminal muramidase (catalytic) domain and act in a

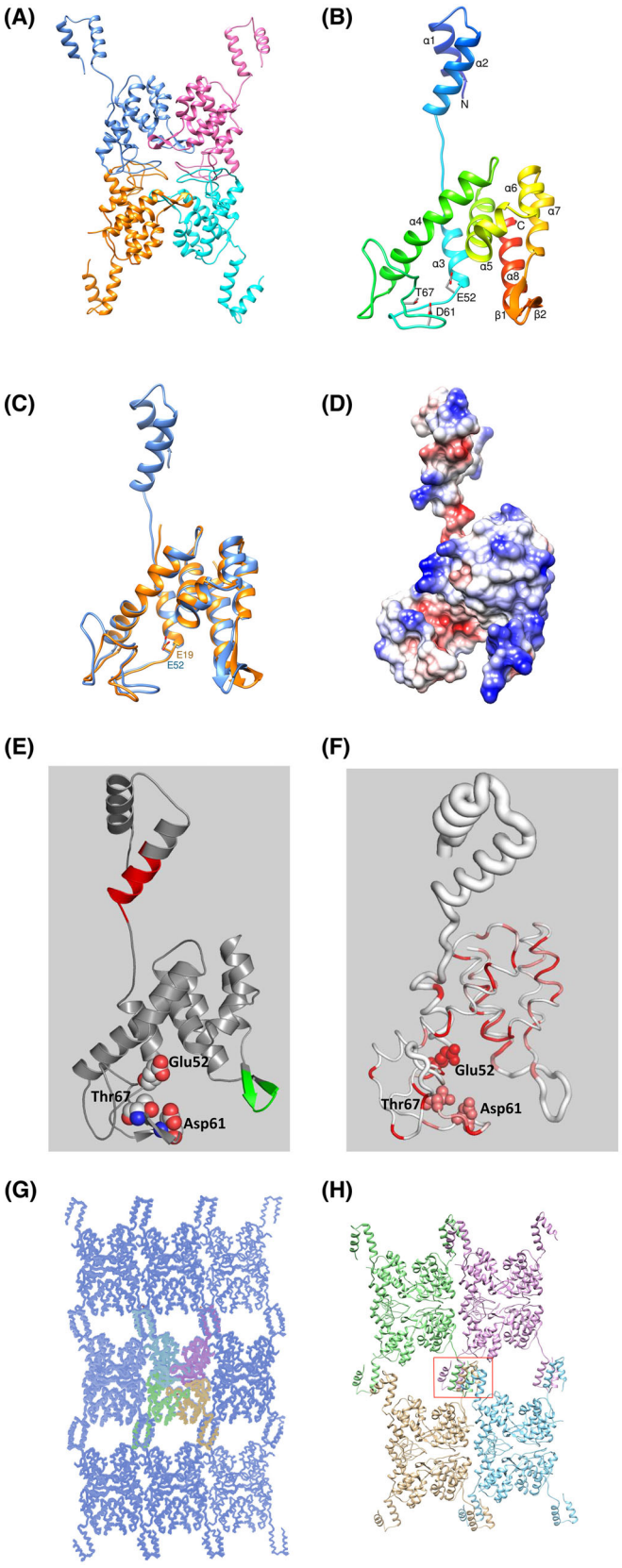

Fig. 8. Crystal structure of *Ab*Lys1. (A) Arrangement of the four *Ab*Lys1 molecules in the crystallographic asymmetric unit. Each *Ab*Lys1 molecule is shown in a different colour, (B) ribbon diagram of *Ab*Lys1 structure in rainbow colouring from N- to C-terminal. The three conserved catalytic amino acids (Glu52, Asp61 are Thr67) are shown. Secondary structure elements were assigned by Chimera [70] as follows: α1: residues 4–13, α2: residues 20–33, α3: residues 42–51, α4: residues 89–110, α5: residues 117–136, α6: residues 139–146, α7: residues 149–158. α8: 172–185, β1: 161–164 andβ2: 167–170. (C) Structural superposition of *Asticcacaulis excentricus* Spmx (PDB id 6h9d) onto *Ab*Lys1. The catalytic Glu residue in both structures is shown in a stick representation. (D) Electrostatic surface representation of *Ab*Lys1. (E) Ribbon diagram of *Ab*Lys1 structure. The sequences with predicted antimicrobial activity at the antenna (AMseq1) and β-hairpin (AMseq2) regions are coloured in red and green, respectively. The active site residues are presented in ball and stick and coloured according to the atom type. (F) 'Sausage' PYMOL [36] representation showing a tube depiction of *Ab*Lys1 structure where the tube radius is proportional to the mean rms deviation per residue between Cα pairs (flexibility). The tube is coloured according to the level of sequence conservation, from white (low score) to red (identity). The active site residues are presented in ball and stick. (G) Overview of the crystal packing. Symmetry molecules are shown in blue. Molecules of the tetramer are depicted in different colours. (H) Ribbon diagram showing the interactions of molecule B N-terminal domain (brown) with symmetry molecules A (cyan), D (green) and C (cyan). Figures A, B, C, D and H were created with Chimera, G was created with Coot and E and F with PYMOL.

similar fashion as a SAR domain to facilitate membrane anchoring of the *Ab*Lys1.

The N-terminal domain participates in interactions with symmetry molecules in the crystal. Analysis of crystal packing shows that the N-terminal domain is sandwiched between the N-terminal domains of two symmetry molecules and makes a few interactions with the loops 113–115 and 145–149 of a third symmetry molecule (Fig. 8G,H). It is possible that the conformation of the N-terminal domain seen in the crystal structure is also present in the solution, thus facilitating the crystal formation.

In silico analysis of the N-terminal helical domain for putative antimicrobial peptides using the AI4AMP [50], the Antimicrobial Peptide Scanner [51] and the AMPpred algorithms [52] showed that the sequence 26–35 (LNKVVNRLVP) (AMseq1) displays high antimicrobial activity. This sequence is composed of two positively charged residues, provided by arginine and lysine, and a large proportion (60%) of hydrophobic residues. This region may provide a recognition moiety for anchoring/association of the catalytic domain to the outer membrane. Its interaction with the membrane can cause long-lived transitions, thus facilitating the catalytic domain to contact peptidoglycan. Another feature of the antenna-like structure is the presence of the two highly exposed to the solvent arginine residues (Arg11 and Arg17). Those arginine residues may provide the antenna-like structure with two additional attachment points to the outer membrane.

The catalytic residue Glu52 is located in the loop that connects the α3 and α4 helices. The location of Glu52 in the loop indicates the requirement for flexibility and plasticity for catalysis (Fig. 8F). This plasticity is probably required for effective binding to the outer membrane for gaining access to peptidoglycan. Several Gly residues are present in the structure giving rise to high flexibility. For example, Gly residues at positions 15 and 16 give flexibility to the loop connecting helices α1 and α2. Gly44 at the C-terminal part of the linker structure, which connects the catalytic domain with the exposed antenna-like structure, contributes further to the high flexibility of the structure (Fig. 8F).

The muramidase/catalytic domain of the protein is rich in positive amino acid residues. This prompted us to *in silico* investigate the presence of putative antimicrobial sequences. Prediction of the antimicrobial activity of the enzyme using the AI4AMP algorithm [50] showed that the C-terminal region 101–187 displays a putative antimicrobial activity. The antimicrobial activity was also confirmed by the Antimicrobial Peptide Scanner [51] and AMPpred [52] algorithms. This region is formed by α-helices and is composed of a large number of positive residues (the total composition of Arg and Lys residues of this particular region is about 17%). The predicted isoelectric point is 9.93. *In silico* analysis of the putative short peptides derived from this region showed that the region 162–169 (GRVKGKL) (AMseq2) displays stronger antibacterial activity, as predicted by the three different algorithms used for the evaluation of the activity. Inspection of the amino acid sequence alignments (Fig. 1B) shows that this region exhibits the lowest homology and forms a β-hairpin. Furthermore, it is exposed to the solvent and lying opposite to the active site residues (Fig. 8D). Noteworthy, this region is only found in viral-type lysozymes (endolysins) and is absent in the autolysin-type lysozymes; therefore, it can be used as a motif for their identification. Presumably, this region is used by the viral-type lysozymes not only for achieving the formation of the substrate-binding pocket but also for providing a synergistic antibacterial activity. Its high *in silico* predicted antibacterial activity suggests that it may act as a surfactant-like peptide [53], providing an initial point of association with the outer

membrane of Gram-negative bacteria [54]. Insertion of this region into the outer membrane can induce perturbing effects on the bilayer structure, making the peptidoglycan more accessible to the active site. The 3D structure of this β-hairpin shows high similarity with the antimicrobial peptide gomesin [55]. Furthermore, two additional structural features must be underlined. The first feature is its contribution to the strong positive electrostatic potential of this region, achieved by three positively charged amino acids (Arg163, Lys165 and Lys167; Fig. 8E). The second feature is its high flexibility (Fig. 8F) due to the presence of Gly162 and Gly166. The three positively charged residues adopt a protruding extended conformation, allowing their direct interaction with the cell wall. López Cascales et al. [56] have reported that the first step of the mechanism used by small cationic peptides to exert their antimicrobial activity is determined by the electrostatic interactions between the cationic peptide and the pathogen's cell membrane. Noteworthy, the membrane of Gram-negative bacteria (such as *A. baumannii*) is negatively charged due to the presence of exopolysaccharides [57,58]. Gram-negative bacteria have an outer membrane with an inner leaflet containing only phosphatidic acid and an outer leaflet made of lipopolysaccharide (LPS). LPS has negatively charged phosphate groups that combine with a salt bridge provided by a divalent cation (e.g. Ca^{2+} and Mg^{2+}) to form an electrostatic zone [59]. This electrostatic area makes the Gram-negative bacteria less permeable and appears to be the main barrier against hydrophobic antibiotics.

Construction of truncated forms of *Ab*Lys1, expression and purification of the engineering variants

To evaluate whether the predicted sequences AMseq1 and AMseq2 indeed contribute to the antimicrobial activity of *Ab*Lys1, three truncated variants of the enzyme were designed and PCR constructed: (a) *Ab*Lys1TruAMseq1, lacking the AMseq1; (b) *Ab*Lys 1TruAMseq2, lacking the AMseq2; and (c) *Ab*Lys1 TruAMseq1seq2, where both antimicrobial sequences were deleted. The three enzyme variants were expressed and purified as described for the wild-type enzyme and the catalytic and antimicrobial activity of purified proteins were assessed. The results, depicted in Fig. 9, showed that the AMseq1 and AMseq2 appear to have little effect on *Ab*Lys1 lytic activity when purified peptidoglycan is used as substrate (Fig. 9A). This is an expected outcome considering that both sequences AMseq1 and AMseq2 were predicted to have surfactant-like properties [53], providing anchoring points for the association of the enzyme with the outer membrane of Gram-negative bacteria [54]. On the other hand, when the lytic activity was assessed using cell suspensions (Fig. 9B, Table 3), the truncated enzymes displayed substantial altered lytic activity. In particular, AMseq2 appears to affect stronger the enzyme's lytic activity compared to AMseq1. The lytic activity of the enzyme variant *Ab*Lys1TruAMseq1seq2, where both antimicrobial sequences were deleted, was affected even more strongly (Table 3), suggesting a possible synergistic function of AMseq1 and AMseq2.

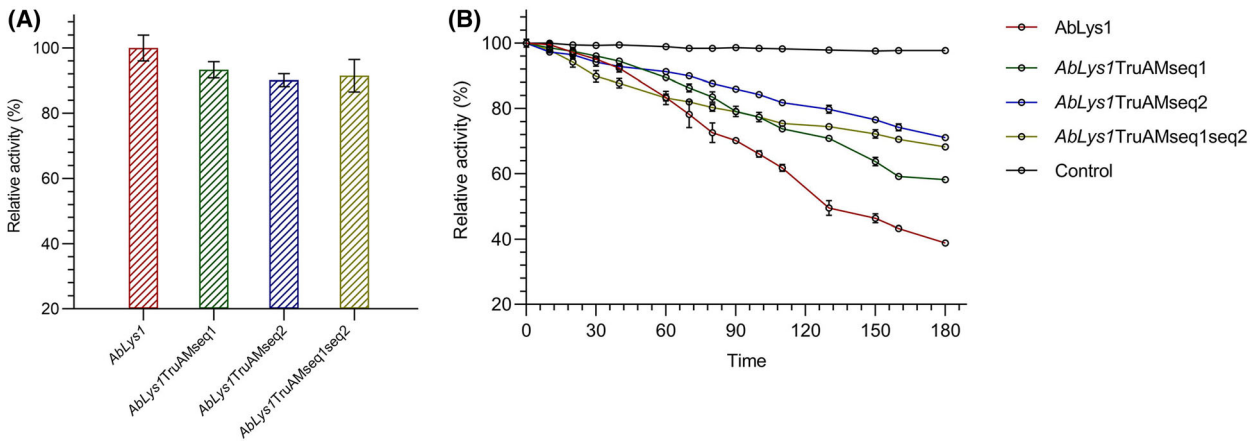

Fig. 9. (A) Relative enzyme activity of the recombinant *Ab*Lys1 and the truncated variants *Ab*Lys1TruAMseq1, *Ab*Lys1TruAMseq2 and *Ab*Lys1TruAMseq1seq2. Enzyme activity was demonstrated by using as substrate RBBR-PNG. Error bars represent the estimated standard deviation. (B) Enzyme activity was demonstrated by measuring the time-dependent turbidity changes in a suspension of *A. baumannii* cells. Changes in turbidity were measured at 600 nm at regular time intervals and a fixed temperature (25 °C), using purified *Ab*Lys1, *Ab*Lys1TruAMseq1, *Ab*Lys1TruAMseq2 and *Ab*Lys1TruAMseq1seq2, compared to a negative control in the absence of the enzyme. Error bars represent the estimated standard deviation.

Table 3. The catalytic activity and the T_m of the truncated forms of *Ab*Lys1.

Enzyme	Lytic activity (units·mg^{-1})	T_m (°C)
*Ab*Lys1	252.7	45.81 ± 0.03
*Ab*Lys1TruAMseq1	214.7	49.39 ± 0.04
*Ab*Lys1TruAMseq2	110.4	45.03 ± 0.02
*Ab*Lys1TruAMseq1seq2	102.5	47.43 ± 0.06

The role of the AMseq1 and AMseq2 sequences on enzyme stability was also evaluated. The enzyme variants were subjected to DSF and the melting point of each variant was determined. The results are presented in Fig. 5A and the measured T_m values are listed in Table 3. A diverse effect of the AMseq1 and AMseq2 sequences on enzyme's structural stability was observed. The *Ab*Lys1TruAMseq1 appears to display higher stability (49.39 ± 0.04 °C) compared to the wild-type enzyme, whereas *Ab*Lys1TruAMseq2 lower stability (45.03 ± 0.02 °C). The T_m of the double variant lies between the other two variants. The unexpected higher stability of the *Ab*Lys1TruAMseq1 enzyme is difficult to be explained based on our available structural data; however, we can speculate that dynamics or entropic aspects may contribute to the observed higher thermostability. Presumably, the flexibility of the antenna-like domain was reduced because of the deletion. On the other hand, the omission of the AMseq2 sequence in the *Ab*Lys1TruAMseq2 variant probably alters the relevant orientation of the helix α7 and helix α8. The deletion of Gly162 and Gly166 may provide restrictions to helices α7 and α8 for adopting optimum conformations, thus leading to a less stable enzyme.

Conclusions

Endolysins based on natural or engineered sequences represent one of the most exciting new strategies for developing novel antimicrobial agents in the face of burgeoning antibiotic resistance and a decline in the discovery of new antibiotics. Phages have evolved several classes of endolysins aiming at degrading the cell wall of their bacterial hosts. The *A. baumannii* bacteriophage AbTZA1 endolysin belongs to the GH24 family. *Ab*Lys1 exhibits a high ability to kill *A. baumannii* cells and inhibit their growth, suggesting that it may possess a therapeutic potential as an alternative antimicrobial agent. Structural and functional studies revealed a unique mechanism for *A. baumannii* recognition and lysis. The crystal structure of *Ab*Lys1 was determined by X-ray crystallography to 1.82 Å resolution, allowing the delineation of the hydrolytic and molecular recognition mechanisms exploited by the enzyme to attack *A. baumannii*. The *Ab*Lys1 structure revealed two helical domains: a small, antenna-like, N-terminal domain with two α-helices (α1 and α2) and a larger C-terminal domain with six α-helices and two short β-strands that form a β-hairpin. Both the antenna-like, N-terminal domain and the β-hairpin have regions (AMseq1 and AMseq2) with predicted antimicrobial activity. Mutagenesis studies revealed the key roles of these regions on the lytic activity of *Ab*Lys1 towards bacterial cells but not towards purified peptidoglycan. These results suggest that AMseq1 and AMseq2 provide synergistic roles in *Ab*Lys1 function presumably by helping the catalytic domain to anchor on the cell wall. These regions also affect the thermostability of *Ab*Lys1.

Materials and methods

Bacterial strains

The *A. baumannii* strain used in this study was isolated in the Department of Microbiology, 'Aghia Sophia' Children's Hospital, Athens. An antibiogram was conducted and revealed that this strain exhibits the following characteristics concerning antibiotic resistance (where: S, susceptible; R, resistant): Amikacin S, Ciprofloxacin R, Colistin S, Gentamicin R, Imipenem S, Meropenem S and Tobramycin S.

Staphylococcus aureus ATCC™ 25923 and *Enterococcus faecalis* ATCC™ 29212 were obtained from Microbiologics (St. Cloud, MN, USA). *Streptococcus pyogenes*, *Bacillus cereus* and *Clostridium difficile* were isolated and obtained as clinical strains from the Department of Microbiology, 'Aghia Sophia' Children's Hospital, Athens.

Sequence mining, synthesis and cloning of *Ab*Lys1 from Acinetobacter phage *Ab*TZA1

The sequence coding for a hypothetical glycoside hydrolase-like protein was identified (Accession No: AZU98615.1) from Acinetobacter phage *Ab*TZA1 (GenBank: MK278860.1) and obtained as a synthetic gene (Eurofins Genomics, Abersberg, Germany). PCR was performed to amplify the full-length ORF of the gene. The primers sequences were as follows: 5′-GAAGGAGATATACATATGGACGTCAAACCGTTCT TTG-3′ and 5′-ATGGTGGTGATGATGTTGTTCGAAAT ACGCTTTCTCTTTC-3′. The PCR reaction was carried out in a total volume of 25 µL. PCR contained 10 µM of each primer, 20 ng template DNA, 0.25 mM of each dNTP, 5 µL of 5× KAPA HiFi Fidelity buffer and 0.5 units (U) of KAPA HiFi DNA polymerase (KAPA Biosystems, Wilmington, Delaware, USA). The PCR protocol was comprised of 30 cycles. Initial template denaturation was performed for 3 min at 95 °C, followed by 30 cycles of 20 s at 98 °C, 15 s at 64 °C and 15 s at

72 °C. A final extension step at 72 °C for 10 min was implemented after the 30th cycle. The resulting PCR amplicon was ligated into the pETite (Lucigen, Middleton, Wisconsin, USA) expression vector. The resulting expression construct pETite-*Ab*Lys1-6xHis was verified by Sanger sequencing and was used to transform *E. coli* BL21 (DE3) cells.

Heterologous expression in *E. coli* BL21 (DE3) and purification of *Ab*Lys1

Transformed *E. coli* BL21 (DE3) cells harbouring the pETite-*Ab*Lys1-6xHis plasmid were grown at 37 °C in 1 L LB medium (tryptone, 1% w/v; yeast extract, 0.5% w/v; NaCl, 1% w/v) containing 30 $\mu g \cdot mL^{-1}$ kanamycin. The expression of *Ab*Lys1 was induced by the addition of isopropyl 1-thio-β galactopyranoside (IPTG, 1 mM) when the absorbance at 600 nm was approximately 0.5–0.6. Four hours after induction, cells were harvested by centrifugation at 8000 ***g*** for 10 min (4 °C). Cells were resuspended in lysis buffer (50 mM sodium phosphate buffer, pH 8.0) containing sodium chloride (0.3 M) and imidazole (10 mM). The suspension was sonicated and centrifuged (12 000 ***g*** for 10 min) and the clear solution was loaded to a column of Ni^{+2}-IDA-Sepharose (0.5 mL), which was previously equilibrated with sodium phosphate buffer (50 mM, pH 8.0), containing sodium chloride (0.3 M) and imidazole (10 mM). Non-absorbed protein was washed-off with 10 mL equilibration buffer. Bound *Ab*Lys1 was eluted with an equilibration buffer containing various concentrations of imidazole (50, 100, 150, 250 and 350 mM). Collected fractions were assayed for protein [60]. Protein purity was judged by SDS/PAGE and the fractions with the highest purity (elution with 150–350 mM imidazole) were mixed and stored at 4 °C.

Differential Scanning Fluorimetry (DSF)

DSF uses the extremely sensitive SYPRO™ Orange dye for monitoring the thermal denaturation of a protein. When the fluorescence intensity is described as a function of temperature, the resulting graph results in a sigmoidal curve, the mean of which describes the temperature (T_m) at which the two forms of the protein (folded and unfolded) are equal in the mixture [61]. For the melting curves of the proteins, which have one denaturation step, the T_m is described by the Boltzmann sigmoidal equation and defined as its turning point. Boltzmann equation is as follows:

$$y = \mathrm{LL} + \frac{(\mathrm{UL} - \mathrm{LL})}{1 + e^{\frac{(Tm - T)}{\alpha}}}$$

Where T is the temperature (°C); y, the fluorescence intensity; LL and UL are the lower and upper limits of the sigmoidal curve used to calculate the T_m (lower and upper fluorescence intensity); and α is the slope of the curve. The melting curves (increase in fluorescence) were monitored using a real-time PCR instrument (StepOne, Thermo Fisher Scientific, Waltham, MA, USA) using a ROX filter. Samples were heated from 25 to 95 °C at a constant rate of 1 $°C \cdot min^{-1}$. Apparent melting temperatures (T_m, app) were calculated as an inflection point of the melting curve, assuming a two-state unfolding model, using the Protein Thermal Shift software (T_mD in the software, Thermo Fisher Scientific). Assays were performed in triplicate.

Purification of *A. baumannii* cell wall peptidoglycan and labelling with Remazol Brilliant Blue-R

Peptidoglycan from *A. baumannii* cells was isolated as previously described [62] with some minor modifications. Immediately after reaching the stationary phase, the culture was subjected to thermal inactivation (121 °C, 30 min). Following purification, peptidoglycan from *A. baumannii* was lyophilized and stored at −20 °C.

The labelling procedure of peptidoglycan from *A. baumannii* cells with Remazol Brilliant Blue-R (RBBR) was carried out using the protocol described by Zhou et al. [63], with minor modifications. Insoluble peptidoglycan (0.5 g) was suspended in 30 mL NaOH (0.25 M) containing RBBR in a final concentration of 0.02 M. The mixture was incubated at 37 °C for 6 h. After incubation, labelled peptidoglycan was harvested by centrifugation at 9000 ***g*** for 10 min, followed by several times of washing with MilliQ distilled water until the filtrate appeared colourless. RBBR-PNG complex was lyophilized and stored at −20 °C.

Remazol Brilliant Blue-R-labelled peptidoglycan degradation assay

The RBBR-labelled peptidoglycan (RBBR-PNG) degradation assay was conducted as described by Santin and Cascales with minor modifications [64]. Incubation mixtures (1 mL) containing *Ab*Lys1 (150 μg) and the RBBR-PNG complex (0.5 $mg \cdot mL^{-1}$) were prepared in an appropriate buffer to give an OD_{595nm} of 0.1–0.2. Mixtures were incubated at 25 °C for 2 h. OD_{595nm} was recorded at 5 min intervals.

Effect of temperature and pH on *Ab*Lys1 activity

Determination of the optimum pH activity was performed using the RBBR-PNG assay in each pH value as described above. The effect of pH was evaluated using the following buffer systems (0.05 M): Glycine-HCl, pH 3; CH_3COONa, pH 4; CH_3COONa, pH 5; MES pH 6; MES, pH 6.5; HEPES, pH 7.0; HEPES, pH 7.5; HEPES, pH 8.0; Glycine-NaOH, pH 9.0; and Glycine-NaOH, pH 10.0. To analyse the temperature stability of *Ab*Lys1, 150 μg of purified enzyme was pre-incubated in HEPES buffer (0.05 M, pH 7.5) at different temperatures over a 10-min period followed by cooling on ice for 5 min. The enzyme activity was measured using the RBBR-PNG assay.

Measurement of glycosidase activity of *AbLys1*

Briefly, incubation mixtures (1 mL) were prepared in HEPES, 50 mM, pH 7.5, containing *Ab*Lys1 (50 μg) and *A. baumannii* cell walls to a final OD_{600nm} of 0.6. Mixtures were incubated at room temperature for 2 h and incubation was terminated by heat at 100 °C for 5 min. The reducing groups, liberated by the cleavage of glycosidic bonds in the peptidoglycan glycan chain, stoichiometrically reduce ferricyanide to ferrocyanide. Undigested cell walls were pelleted by centrifugation at 13 000 ***g*** for 15 min. Cell wall digests were assayed for cleavage of the peptidoglycan polysaccharide backbone using the Park–Johnson method [37]. The experiments were performed in triplicate. Different concentrations of glucose (0–6 $\mu g \cdot mL^{-1}$) were used for constructing the standard curve.

Antimicrobial activity of *Ab*Lys1 using turbidity assays

In order to determine whether *Ab*Lys1 can exert antimicrobial activity against six bacterial species (*A. baumannii*, *E. faecium*, *S. aureus*, *S. pyogenes*, *B. cereus* and *C. difficile*), turbidity assays were used. In brief, overnight cultures of each bacteria stain were thermally deactivated (121 °C, 30 min) and bacteria cells were harvested through centrifugation (8000 ***g***). Suspensions of each strain containing 150 μg of *Ab*Lys1, in HEPES buffer (pH 7.5, 50 mM), were prepared in order to achieve a turbidity equivalent of 0.5–0.6 (A_{600nm}). Reactions were incubated at room temperature for 2 h and the reduction in OD_{600nm} was recorded every 10 min.

Antimicrobial activity assays using the disc diffusion method

To determine the antimicrobial activity of *Ab*Lys1 against the clinical *A. baumannii* strain, the Kirby–Bauer disc diffusion method in agar was used [65]. Mueller–Hinton (MH) (ThermoScientific™ OXOID™) agar plates were inoculated with *A. baumannii* inoculum prepared by making a direct buffer suspension of isolated colonies selected from an 18–24 h MH agar plate culture. The suspension was adjusted to achieve a turbidity equivalent to a 0.5 McFarland standard and was swabbed uniformly across the MH agar. Then, filter paper discs (6 mm in diameter) containing different concentrations of *Ab*Lys1 were placed on the agar surface. The Petri dishes were incubated at 25 °C for 24 h.

Determination of bactericidal concentration of *Ab*Lys1 by broth dilution method

To set up the broth dilution method, a suspension of *A. baumannii* clinical strain was prepared by making a direct buffer suspension of isolated colonies selected from an 18 to 24 h MacConkey No 2 agar plate culture. The suspension was adjusted to achieve a turbidity equivalent to a 0.5 McFarland turbidity standard, and a suspension containing approximately 10^5 colony forming units (CFU)$\cdot mL^{-1}$ for *A. baumannii* strain was prepared. The suspension was split into six tubes (1 mL final volume) containing different concentrations of *Ab*Lys1. The tubes were incubated for 5 h and 100 μL of each sample was applied on Mueller–Hinton agar plate and incubated at 37 °C for 24 h.

Live/dead bacteria distinction method for evaluation of antibacterial activity of *Ab*Lys1

The antibacterial activity of *Ab*Lys1 was also evaluated by conducting the live/dead bacteria distinction method, using the Bacterial Viability and Gram Stain Kit (Biotium). Bacterial suspensions were incubated in the presence and absence of the *Ab*Lys1 in MH broth for 5 h. After incubation, *A. baumannii* cells were harvested by centrifugation at 10 000 ***g*** for 5 min in microcentrifuge tubes, washed once with 150 mM NaCl by gently pipetting up and down and treated according to the protocol supplied by the manufacturer. Ethidium homodimer III (EthD-III) is a membrane-impermeant nucleic acid binding dye that selectively stains *A. baumannii* cells compromised with plasma membranes after incubation in the presence of *Ab*Lys1. All bacteria cells were stained blue with the membrane-permeant DNA dye, 4′,6-diamidino-2-phenylindole (DAPI). Images have been taken with Zeiss LSM 800 inverted confocal microscope with a Plan-Apochromat 63X/1.40 lens. For DAPI dye the laser parameters were: excitation at 405 nm, detection at 400-585 nm, laser intensity at 1.90 %, detector gain at 1.0.For EthD-III dye the laser parameters were: excitation at 488 nm, detection at 561-700 nm, laser intensity at 3.10 %, detector gain at 1.0. For transmitted light (ESID) parameters were: excitation at 405 nm, laser intensity at 3.50 %. All images have been taken in sequential scanning mode.

Crystallization, structure determination and analysis

Purified *Ab*Lys1 was concentrated at 15 $mg \cdot mL^{-1}$ in buffer HEPES-NaOH 10 mM, NaCl 100 mM and NaN_3 0.002% w/v, pH 7.0. Crystals were grown using the hanging drop vapour diffusion method. The well solution consisted of 0.1 M phosphate/citrate, 0.2 M lithium sulfate and 20% w/v PEG 1000, pH 4.2. Each drop contained 2 μL of protein solution and 2 μL of well solution. The drops were left to equilibrate at 16 °C. Crystals appeared after ~ 10 days but the process was accelerated by seeding [66]. X-ray diffraction data at 100 K using 20% v/v glycerol as cryoprotectant were collected on beamline P13 at PETRA III storage ring (DESY, Hamburg, Germany). Most crystals exhibited high disorder and diffracted to low resolution (5 Å or worse). A data set of 1.82 Å was collected after screening more than 50 crystals and was used for structure determination by molecular replacement. The space group and unit cell

dimensions suggested four *Ab*Lys1 molecules in the crystallographic asymmetric unit. A model of *Ab*Lys1 was constructed with AlphaFold [67], and after modification in Phenix 1.20.1-4487 [68] for proper assignment of B-factors, it was used for molecular replacement as a two-domain search model in Phaser [69]. The initial solution was improved by manual building in Coot 0.9.5 [70] and refinement with Phenix 1.20-4487 using simulated annealing and maximum likelihood as the target. No resolution cut-off was applied in the data as map and structure quality improved when all data were included in the calculations. X-ray data collection and final refinement statistics are given in Table 1.

Bioinformatics and structure analysis

For the inspection of models and crystal structures, the program PYMOL [71] was used. Sequences homologous to *Ab*Lys1 were sought in the PDB using BLASTp [72]. The resulting sequence set was aligned with CLUSTAL OMEGA [73]. ESPript and ENDscript (http://espript.ibcp.fr) were used for alignment visualization and analysis [74]. Structure comparison was achieved using PDBePISA [75]. Prediction of the antimicrobial activity was carried out using three algorithms: AI4AMP [50], Antimicrobial Peptide Scanner [51] and AMPpred algorithms [52]. Multiple sequence alignment was achieved using Cobalt [76]. The phylogenetic tree was constructed with Phylip and displayed with ITOL v4 [77].

Construction of truncated forms of *Ab*Lys1 and expression and purification of the engineering variants

The procedure for the removal of the potential antimicrobial sequences and construction of the truncated forms of *Ab*Lys1 consisted of the following steps: Firstly, the construction of the gene without the antimicrobial sequences was performed with suitably designed primers by amplifying the initial plasmid containing the whole *Ab*Lys1 gene. The amplification was performed with a high-fidelity polymerase following the manufacturer's protocol (25 μL final volume). The following primers were used for the removal of AMseq1 and AMseq2 sequences, respectively: 5′ GATGACGTGGATATCTCCGATC 3′, 5′ GAGGTTATTCCAGGCCTGAC 3′. The final PCR products were linear plasmid vectors without the nucleotide sequences of the antimicrobial sequence AMseq1 and AMseq2. Reaction with ligase was followed by adding 2 μL of the PCR product, 1 μL of 10× ligase reaction solution, 6 μL of sterile ddH_2O and 1 μL of T4 DNA ligase (350 $U{\cdot}\mu L^{-1}$). The mixture was incubated at 16 °C for 16 h and enzyme inactivation was performed at 65 °C for 15 min. The next step was the removal of vectors carrying the parental genes by DpnI restriction enzyme by adding 1.5 μL of 10× DpnI buffer and 0.5 μL DpnI (10 $U{\cdot}\mu L^{-1}$) to ligation products. The mixture was incubated for 3.5 h at 37 °C and the reaction was stopped at 80 °C for 20 min. The final reaction product was used to transform *E. coli* BL21 (DE3) cells. DNA sequencing was used to confirm the construction of the truncated *Ab*Lys1 variants. Transformed *E. coli* BL21 (DE3) cells were grown at 37 °C in LB medium containing 30 $\mu g{\cdot}mL^{-1}$ kanamycin. The expression of truncated variants was induced by the addition of IPTG (1 mM). Cells were harvested by centrifugation at 8000 ***g*** for 10 min (4 °C). The truncated *Ab*Lys1 variants were purified with affinity chromatography using a column of Ni^{+2}-IDA-Sepharose (0.5 mL) as described for the wild-type enzyme.

Acknowledgements

The research work was supported by the Hellenic Foundation for Research and Innovation (H.F.R.I.) under the 'First Call for H.F.R.I. Research Projects to support Faculty members and Researchers and the procurement of high-cost research equipment grant' (Project Number: 4036). ACP acknowledges infrastructure support from Biocenter Finland and the Academy of Finland. ACP thanks Michael Agthe for assistance during data collection on the EMBL P13 beamline at the PETRA III storage ring (DESY). Access to synchrotron beamtime was provided by European Union's Horizon 2020 project iNEXT-Discovery (grant agreement no. 871037).

Conflict of interest

The authors declare no conflict of interest.

Author contributions

GEP performed all experiments, analysed data and wrote the manuscript; AS, performed experiments and contributed reagents and other essential material; ACP collected X-ray diffraction data, analysed the X-ray structure and wrote the manuscript; and NEL planned experiments, supervised the experiments, analysed data and wrote the manuscript.

Data availability statement

All data are included in the article. The Protein Data Bank accession number for the AbLys1 crystal structure reported in this study is PDB: 8APP.

References

1 Antimicrobial Resistance Collaborators. Global burden of bacterial antimicrobial resistance in 2019: a systematic analysis. *Lancet*. 2022;**399**:629–55.

2 Price R. O'Neill report on antimicrobial resistance: funding for antimicrobial specialists should be improved. *Eur J Hosp Pharm*. 2016;**23**:245–7.
3 Tacconelli E, Carrara E, Savoldi A, Harbarth S, Mendelson M, Monnet DL, et al. Discovery, research, and development of new antibiotics: the WHO priority list of antibiotic-resistant bacteria and tuberculosis. *Lancet Infect Dis*. 2018;**18**:318–27.
4 Chusri S, Chongsuvivatwong V, Rivera JI, Silpapojakul K, Singkhamanan K, McNeil E, et al. Clinical outcomes of hospital-acquired infection with *Acinetobacter nosocomialis* and *Acinetobacter pittii*. *Antimicrob Agents Chemother*. 2014;**58**:4172–9.
5 Garnacho-Montero J, Timsit JF. Managing *Acinetobacter baumannii* infections. *Curr Opin Infect Dis*. 2019;**32**:69–76.
6 Peleg AY, Seifert H, Paterson DL. *Acinetobacter baumannii*: emergence of a successful pathogen. *Clin Microbiol Rev*. 2008;**21**:538–82.
7 Sarshar M, Behzadi P, Scribano D, Palamara AT, Ambrosi C. *Acinetobacter baumannii*: an ancient commensal with weapons of a pathogen. *Pathogens*. 2021;**10**:387.
8 Morris FC, Dexter C, Kostoulias X, Uddin MI, Peleg AY. The mechanisms of disease caused by *Acinetobacter baumannii*. *Front Microbiol*. 2019;**10**:1601.
9 Vallenet D, Nordmann P, Barbe V, Poirel L, Mangenot S, Bataille E, et al. Comparative analysis of acinetobacters: three genomes for three lifestyles. *PLoS One*. 2008;**3**:e1805.
10 Knapp S, Wieland CW, Florquin S, Pantophlet R, Dijkshoorn L, Tshimbalanga N, et al. Differential roles of CD14 and toll-like receptors 4 and 2 in murine *Acinetobacter pneumonia*. *Am J Respir Crit Care Med*. 2006;**173**:122–9.
11 Erridge C, Moncayo-Nieto OL, Morgan R, Young M, Poxton IR. *Acinetobacter baumannii* lipopolysaccharides are potent stimulators of human monocyte activation via toll-like receptor 4 signalling. *J Med Microbiol*. 2007;**56**:165–71.
12 March C, Regueiro V, Llobet E, Moranta D, Morey P, Garmendia J, et al. Dissection of host cell signal transduction during *Acinetobacter baumannii* – triggered inflammatory response. *PLoS One*. 2010;**5**:e10033.
13 Ripa M, Galli L, Poli A, Oltolini C, Spagnuolo V, Mastrangelo A, et al. Secondary infections in patients hospitalized with COVID-19: incidence and predictive factors. *Clin Microbiol Infect*. 2021;**27**:451–7.
14 Chen N, Zhou M, Dong X, Qu J, Gong F, Han Y, et al. Epidemiological and clinical characteristics of 99 cases of 2019 novel coronavirus pneumonia in Wuhan, China: a descriptive study. *Lancet*. 2020;**395**:507–13.
15 Wang Z, Yang B, Li Q, Wen L, Zhang R. Clinical features of 69 cases with coronavirus disease 2019 in Wuhan, China. *Clin Infect Dis*. 2020;**71**:769–77.
16 Gordillo Altamirano FL, Barr JJ. Phage therapy in the postantibiotic era. *Clin Microbiol Rev*. 2019;**32**:1–25.
17 LaVergne S, Hamilton T, Biswas B, Kumaraswamy M, Schooley RT, Wooten D. Phage therapy for a multidrug-resistant *Acinetobacter baumannii* Craniectomy site infection. *Open Forum Infect Dis*. 2018;**5**:1–3.
18 Nelson D, Loomis L, Fischetti VA. Prevention and elimination of upper respiratory colonization of mice by group a streptococci by using a bacteriophage lytic enzyme. *Proc Natl Acad Sci USA*. 2001;**98**:4107–12.
19 Schmelcher M, Donovan DM, Loessner MJ. Bacteriophage endolysins as novel antimicrobials. *Future Microbiol*. 2012;**7**:1147–71.
20 Young R. Bacteriophage lysis: mechanism and regulation. *Microbiol Rev*. 1992;**56**:430–81.
21 Fischetti VA. Bacteriophage lysins as effective antibacterials. *Curr Opin Microbiol*. 2008;**11**:393–400.
22 Fenton M, Ross P, Mcauliffe O, O'Mahony J, Coffey A. Recombinant bacteriophage lysins as antibacterials. *Bioeng Bugs*. 2010;**1**:9–16.
23 Szweda P, Schielmann M, Kotlowski R, Gorczyca G, Zalewska M, Milewski S. Peptidoglycan hydrolases-potential weapons against *Staphylococcus aureus*. *Appl Microbiol Biotechnol*. 2012;**96**:1157–74.
24 Vermassen A, Leroy S, Talon R, Provot C, Popowska M, Desvaux M. Cell wall hydrolases in bacteria: insight on the diversity of cell wall amidases, glycosidases and peptidases toward peptidoglycan. *Front Microbiol*. 2019;**10**:331.
25 Khan FM, Gondil VS, Li C, Jiang M, Li J, Yu J, et al. A novel *Acinetobacter baumannii* bacteriophage Endolysin LysAB54 with high antibacterial activity against multiple gram-negative microbes. *Front Cell Infect Microbiol*. 2021;**11**:1–9.
26 Abdelkader K, Gutiérrez D, Grimon D, Ruas-Madiedo P, Lood C, Lavigne R, et al. Lysin LysMK34 of *Acinetobacter baumannii* bacteriophage PMK34 has a turgor pressure-dependent intrinsic antibacterial activity and reverts colistin resistance. *Appl Environ Microbiol*. 2020;**86**:e01311-20.
27 Chu JJK, Poh WH, Hasnuddin NTB, Hew EY, Dam LC, El Sahili A, et al. Novel phage Lysin Abp013 against *Acinetobacter baumannii*. *Antibiotics*. 2022;**11**:1–13.
28 Nir-Paz R, Gelman D, Khouri A, Sisson BM, Fackler J, Alkalay-Oren S, et al. Successful treatment of antibiotic-resistant, poly-microbial bone infection with bacteriophages and antibiotics combination. *Clin Infect Dis*. 2019;**69**:2015–8.
29 Vasina DV, Antonova NP, Grigoriev IV, Yakimakha VS, Lendel AM, Nikiforova MA, et al. Discovering the potentials of four phage Endolysins to combat gram-negative infections. *Front Microbiol*. 2021;**12**:748718.
30 Vollmer W, Blanot D, De Pedro MA. Peptidoglycan structure and architecture. *FEMS Microbiol Rev*. 2008;**32**:149–67.

31 Oechslin F, Zhu X, Dion MB, Shi R, Moineau S. Phage endolysins are adapted to specific hosts and are evolutionarily dynamic. *PLoS Biol*. 2022;**20**:e3001740.
32 Sykilinda NN, Nikolaeva AY, Shneider MM, Mishkin DV, Patutin AA, Popov VO, et al. Structure of an Acinetobacter broad-range prophage endolysin reveals a C-terminal α-helix with the proposed role in activity against live bacterial cells. *Viruses*. 2018;**10**:309.
33 Danis-Wlodarczyk KM, Wozniak DJ, Abedon ST. Treating bacterial infections with bacteriophage-based enzybiotics: in vitro, in vivo and clinical application. *Antibiotics*. 2021;**10**:1–36.
34 Moak M, Molineux IJ. Peptidoglycan hydrolytic activities associated with bacteriophage virions. *Mol Microbiol*. 2004;**51**:1169–83.
35 Rodríguez-Rubio L, Gutiérrez D, Donovan DM, Martínez B, Rodríguez A, García P. Phage lytic proteins: biotechnological applications beyond clinical antimicrobials. *Crit Rev Biotechnol*. 2016;**36**:542–52.
36 Dams D, Briers Y. Enzybiotics: enzyme-based antibacterials as therapeutics. *Adv Exp Med Biol*. 2019;**1148**:233–53.
37 Pritchard DG, Dong S, Baker JR, Engler JA. The bifunctional peptidoglycan lysin of *Streptococcus agalactiae* bacteriophage B30. *Microbiology*. 2004;**150**:2079–87.
38 Bartik K, Redfield C, Dobson CM. Measurement of the individual pKa values of acidic residues of hen and Turkey lysozymes by two-dimensional 1H NMR. *Biophys J*. 1994;**66**:1180–4.
39 Nielsen JE, McCammon JA. Calculating pKa values in enzyme active sites. *Protein Sci*. 2003;**12**:1894–901.
40 Bustamante N, Rico-Lastres P, García E, García P, Menéndez M. Thermal stability of Cpl-7 Endolysin from the *Streptococcus pneumoniae* bacteriophage Cp-7; Cell Wall-targeting of its CW_7 motifs. *PLoS One*. 2012;**7**:e46654.
41 Heselpoth RD, Owens JM, Nelson DC. Quantitative analysis of the thermal stability of the gamma phage endolysin PlyG: a biophysical and kinetic approach to assaying therapeutic potential. *Virology*. 2015;**477**:125–32.
42 Xu M, Arulandu A, Struck DK, Swanson S, Sacchettini JC, Young R. Disulfide isomerization after membrane release of its SAR domain activates P1 lysozyme. *Science*. 2005;**307**:113–7.
43 Kuroki R, Weaver LH, Matthews BW. A covalent enzyme-substrate intermediate with saccharide distortion in a mutant T4 lysozyme. *Science*. 1993;**262**:2030–3.
44 Akhterov MV, Choi Y, Olsen TJ, Sims PC, Iftikhar M, Gul OT, et al. Observing lysozymes closing and opening motions by high-resolution single-molecule enzymology. *ACS Chem Biol*. 2015;**10**:1495–501.
45 Gálvez-Iriqui AC, Plascencia-Jatomea M, Bautista-Baños S. Lysozymes: characteristics, mechanism of action and technological applications on the control of pathogenic microorganisms. *Rev Mex Fitopatol Mex J Phytopathol*. 2020;**38**:360–83.
46 Love MJ, Abeysekera GS, Muscroft-Taylor AC, Billington C, Dobson RCJ. On the catalytic mechanism of bacteriophage endolysins: opportunities for engineering. *Biochim Biophys Acta Proteins Proteom*. 2020;**1868**:140302.
47 Kuroki R, Weaver LH, Matthews BW. Structural basis of the conversion of T4 lysozyme into a transglycosidase by reengineering the active site. *Proc Natl Acad Sci USA*. 1999;**96**:8949–54.
48 Randich AM, Kysela DT, Morlot C, Brun YV. Origin of a Core bacterial gene via Co-option and detoxification of a phage Lysin. *Curr Biol*. 2019;**29**:1634–1646.e6.
49 Sun Q, Kuty GF, Arockiasamy A, Xu M, Young R, Sacchettini JC. Regulation of a muralytic enzyme by dynamic membrane topology. *Nat Struct Mol Biol*. 2009;**16**:1192–4.
50 Lin T-T, Yang L-Y, Lu I-H, Cheng W-C, Hsu Z-R, Chen S-H, et al. AI4AMP: an antimicrobial peptide predictor using physicochemical property-based encoding method and deep learning. *mSystems*. 2021;**6**:e0029921.
51 Veltri D, Kamath U, Shehu A. Deep learning improves antimicrobial peptide recognition. *Bioinformatics*. 2018;**34**:2740–7.
52 Meher PK, Sahu TK, Saini V, Rao AR. Predicting antimicrobial peptides with improved accuracy by incorporating the compositional, physico-chemical and structural features into Chou's general PseAAC. *Sci Rep*. 2017;**7**:1–12.
53 Castelletto V, Barnes RH, Karatzas KA, Edwards-Gayle CJC, Greco F, Hamley IW, et al. Arginine-containing surfactant-like peptides: interaction with lipid membranes and antimicrobial Activity. *Biomacromolecules*. 2018;**19**:2782–94.
54 Huan Y, Kong Q, Mou H, Yi H. Antimicrobial peptides: classification, design, application and RESEARCH Progress in multiple fields. *Front Microbiol*. 2020;**11**:582779.
55 Silva PI, Daffre S, Bulet P. Isolation and characterization of gomesin, an 18-residue cysteine-rich defense peptide from the spider *Acanthoscurria gomesiana* hemocytes with sequence similarities to horseshoe crab antimicrobial peptides of the tachyplesin family. *J Biol Chem*. 2000;**275**:33464–70.
56 López Cascales JJ, Zenak S, García De La Torre J, Lezama OG, Garro A, Enriz RD. Small cationic peptides: influence of charge on their antimicrobial Activity. *ACS Omega*. 2018;**3**:5390–8.
57 Gottenbos B, Grijpma DW, Van Der Mei HC, Feijen J, Busscher HJ. Antimicrobial effects of positively charged surfaces on adhering gram-positive and gram-negative bacteria. *J Antimicrob Chemother*. 2001;**48**:7–13.

58 Bertani B, Ruiz N. Function and biogenesis of lipopolysaccharides. *EcoSal Plus*. 2018;**8**. https://doi.org/10.1128/ecosalplus.ESP-0001-2018
59 Nikaido H. Molecular basis of bacterial outer membrane permeability revisited. *Microbiol Mol Biol Rev*. 2003;**67**:593–656.
60 Bradford MM. A rapid and sensitive method for the quantitation microgram quantities of protein utilizing the principle of protein-dye binding. *Anal Biochem*. 1976;**72**:248–54.
61 Pouliou F, Perperopoulou F, Labrou NE. Comparative analysis of two stress-inducible tau class glutathione transferases from Glycine max revealed significant catalytic and structural diversification. *Protein Pept Lett*. 2018;**24**:922–35.
62 Fukushima T, Sekiguchi J. Zymographic techniques for the analysis of bacterial cell wall in bacillus. *Methods Mol Biol*. 2016;**1440**:87–98.
63 Zhou R, Chen S, Recsei P. A dye release assay for determination of lysostaphin activity. *Anal Biochem*. 1988;**171**:141–4.
64 Santin YG, Cascales E. Measure of peptidoglycan hydrolase activity. *Methods Mol Biol*. 2017;**1615**:151–8.
65 Bauer AW, Kirby WM, Sherris JC, Turck M. Antibiotic susceptibility testing by a standardized single disk method. *Tech Bull Regist Med Technol*. 1966;**36**:49–52.
66 Hirvonen M, Papageorgiou AC. Crystallization and preliminary crystallographic analysis of a family 45 endoglucanase from the thermophilic fungus *Melanocarpus albomyces*. *Acta Crystallogr Sect D Biol Crystallogr*. 2002;**58**:336–8.
67 Jumper J, Evans R, Pritzel A, Green T, Figurnov M, Ronneberger O, et al. Highly accurate protein structure prediction with AlphaFold. *Nature*. 2021;**596**:583–9.
68 Liebschner D, Afonine PV, Baker ML, Bunkoczi G, Chen VB, Croll TI, et al. Macromolecular structure determination using X-rays, neutrons and electrons: recent developments in Phenix. *Acta Crystallogr Sect D Struct Biol*. 2019;**75**:861–77.
69 McCoy AJ, Grosse-Kunstleve RW, Adams PD, Winn MD, Storoni LC, Read RJ. Phaser crystallographic software. *J Appl Cryst*. 2007;**40**:658–74.
70 Emsley P, Cowtan K. Coot: model-building tools for molecular graphics. *Acta Crystallogr Sect D Biol Crystallogr*. 2004;**60**:2126–32.
71 Schrödinger L, DeLano W. PyMOL. 2020 [cited 2022 Sep 19]. Available from: http://www.pymol.org/pymol
72 Altschul SF, Gish W, Miller W, Myers EW, Lipman DJ. Basic local alignment search tool. *J Mol Biol*. 1990;**215**:403–10.
73 Sievers F, Wilm A, Dineen D, Gibson TJ, Karplus K, Li W, et al. Fast, scalable generation of high-quality protein multiple sequence alignments using Clustal omega. *Mol Syst Biol*. 2011;**7**:539.
74 Robert X, Gouet P. Deciphering key features in protein structures with the new ENDscript server. *Nucleic Acids Res*. 2014;**42**:320–4.
75 Krissinel E, Henrick K. Inference of macromolecular assemblies from crystalline state. *J Mol Biol*. 2007;**372**:774–97.
76 Papadopoulos JS, Agarwala R. COBALT: constraint-based alignment tool for multiple protein sequences. *Bioinformatics*. 2007;**23**:1073–9.
77 Letunic I, Bork P. Interactive tree of life (iTOL) v4: recent updates and new developments. *Nucleic Acids Res*. 2019;**47**:256–9.